

# Bioinspired Graphene Oxide Membranes with Dual Transport Mechanisms for Precise Molecular Separation

Haozhen Dou, Mi Xu, Bin Jiang, Guobin Wen, Lei Zhao, Baoyu Wang, Aiping Yu, Zhengyu Bai, Yongli Sun, Luhong Zhang,\* Zhongwei Chen,\* and Zhongyi Jiang\*

The implementation of membrane technology to replace or combine with energy-intensive cryogenic distillation for precise separation of ethylene/ethane mixture proves an extremely important yet highly challenging task. Inspired by the hierarchical structure and facilitated gas transport of biological membranes, a highly selective ethylene/ethane separation membrane is explored through the fixation of a silver ion carrier and the impregnation of ionic liquid within 2D nanochannels of graphene oxide laminate, where plenty of ethylene-permeating in-plane nano-wrinkles and ethylene-facilitated plane-to-plane nanochannels are constructed. By virtue of synergistic effects of molecular sieving and carrier-facilitated transport, an unprecedented combination of high ethylene permeance (72.5 GPU) and superhigh ethylene/ethane selectivity (215) is achieved, out-performing currently reported advanced membranes. Moreover, molecular dynamics simulations verify a favorable membrane nanostructure for fast and selective transport of ethylene molecules. This bioinspired approach with dual transport mechanisms may open novel avenues to the design of high-performance membranes for precise molecular separation.

## 1. Introduction

Olefin/paraffin separations are crucial processes in the petrochemical industry, providing largest amount of feedstocks for many chemical products and household plastics.<sup>[1]</sup> Owing to the similar sizes and volatilities of olefin and paraffin molecules, the industrial production of high purity propylene and ethylene is mainly accomplished by the energy-intensive cryogenic distillation, which accounts for 0.3% of global energy consumption.<sup>[2]</sup> Membrane-based separations continue to attract increasing attention for their high energy efficiency, low carbon footprints, operational simplicity, and compact spacing.<sup>[3,4]</sup> In this scenario, enormous efforts have been devoted to the design of diverse types of advanced separation membranes, such as carbon molecular sieve membranes, metal-organic framework (MOF) membranes, ionic liquid (IL) membranes, and deep eutectic solvent

membranes.<sup>[5–7]</sup> However, a distinct trade-off between the selectivity and permeability of these membranes still exists. Meanwhile, the selectivity is far from being commercially attractive, especially for ethylene/ethane separation.<sup>[8,9]</sup>

Recently, 2D laminated membranes have been deemed as new-generation platforms for high-performance separations due to their ultrafast molecular transfer, robust chemical stability, and facile tuning of channel size.<sup>[10]</sup> In particular, graphene oxide (GO) membranes possess tremendous potential for gas sieving, where the molecular transport occurs through in-plane slit-like pores and then plane-to-plane nanochannels.<sup>[11]</sup> By fine-tuning the sizes of slit-like pores and the intrinsic nanochannels, GO membranes have exhibited high selectivity for a number of gas separations, such as H<sub>2</sub>/CO<sub>2</sub>, H<sub>2</sub>/CH<sub>4</sub>, or CO<sub>2</sub>/N<sub>2</sub>.<sup>[12]</sup> However, for the precise molecular separations represented by separation of ethylene/ethane pairs (0.416/0.443 nm), the extremely small size difference of gas pair is particularly challenging for the design of 2D membranes. To acquire high selectivity, other transport mechanisms besides molecular sieving mechanism need to be incorporated.<sup>[13]</sup>

The ultrafast gas transport and superior selectivity of biological membranes grant germane inspiration for the design of highly efficient 2D membranes.<sup>[14]</sup> A variety of specific aquaporins (AQPs) embedded in the lipid bilayer contributes to the highly selective and fast transport of different physiological


Dr. H. Dou, Dr. M. Xu, Prof. B. Jiang, Prof. Y. Sun, Prof. L. Zhang, Prof. Z. Jiang  
School of Chemical Engineering and Technology  
Tianjin University  
Tianjin 300350, China  
E-mail: zhanglvh@tju.edu.cn; zhyjiang@tju.edu.cn

Dr. H. Dou, Dr. G. Wen, Dr. L. Zhao, Prof. A. Yu, Prof. Z. Chen  
Department of Chemical Engineering  
University of Waterloo  
200 University Ave. W, Waterloo, Ontario N2L 3G1, Canada  
E-mail: zhwchen@uwaterloo.ca

Prof. B. Wang  
School of Chemical Engineering and Food Science  
Zhengzhou Institute of Technology  
Zhengzhou 450044, China

Prof. Z. Bai  
School of Chemistry and Chemical Engineering  
Key Laboratory of Green Chemical Media and Reactions  
Henan Normal University  
Xinxiang 453007, China

Prof. Z. Jiang  
Collaborative Innovation Centre of Chemical Science and Engineering  
Key Laboratory for Green Chemical Technology of Ministry of Education  
Tianjin 300350, China

 The ORCID identification number(s) for the author(s) of this article can be found under <https://doi.org/10.1002/adfm.201905229>.

DOI: 10.1002/adfm.201905229

gases through the cell membranes, such as  $\text{CO}_2$ ,  $\text{NO}$ , and  $\text{NH}_3$ .<sup>[15,16]</sup> For example, the  $\text{CO}_2$  permeability of AQP1 can reach up to 1 20 000 molecules per second per AQP1 subunit. The combination of high selectivity and permeability is ascribed to the unique features of AQPs.<sup>[17]</sup> The AQP forms tetramer with each monomer consisting of six bilayer-spanning helices, which are assembled into well-defined nanochannels. On the one hand, the size and shape of these nanochannels enable the gas species to pass through exclusively and achieve molecular sieving.<sup>[18]</sup> On the other hand, the amino terminal and carboxyl terminal of the amino acid sequence symmetrically fixed in the nanochannel surfaces can act as carriers and selectively recognize the target species, thus facilitating desired gas transport both energetically and entropically.<sup>[9,16]</sup> Mimicking the dual transport mechanisms of biological membranes offers a broad perspective and straightforward strategy for the design of 2D membranes to carry out precise molecular separations.

Herein, by imitating dual transport mechanisms of biological membranes, we design and construct a kind of bioinspired GO membrane with synergistic effects of molecular sieving and carrier-facilitated transport for highly efficient ethylene/ethane separation. Owing to the high specific surface area and abundant oxygen-containing functional groups of GO membrane, silver ions, as effective ethylene-transport carrier,<sup>[19]</sup> are easily fixed within 2D nanochannels. Then, the 2D nanochannels

are further decorated by IL with protic acidic property.<sup>[20]</sup> The selected IL is able to ensure the carrier stability and further regulate the size of nanochannels, while its easy-preparation and green solvent properties foster new features of economic feasibility and environmental friendliness.<sup>[21,22]</sup> After the fixation of carrier and decoration of IL, the interactions of GO with IL and carrier generate numerous in-plane slit-like pores, and their sizes can be tailored by the amount of impregnated IL, which achieve molecular sieving. The IL structure, content, and the GO nanosheets govern the carrier efficiency, which affords carrier-facilitated transport within the 2D nanochannels of the membrane. As a result, by virtue of synergistic effects of molecular sieving and carrier-facilitated transport, the Ag/IL-GO membranes exhibit superhigh ethylene/ethane selectivity and high ethylene permeance, out-stripping most of the state-of-art ethylene/ethane separation membranes.

## 2. Results and Discussion

### 2.1. Membrane Design and Fabrication

Single-layered GO nanosheet is prepared by improved Hummers method.<sup>[23]</sup> Afterward, the bioinspired membranes are constructed by the following three steps (Figure 1a):

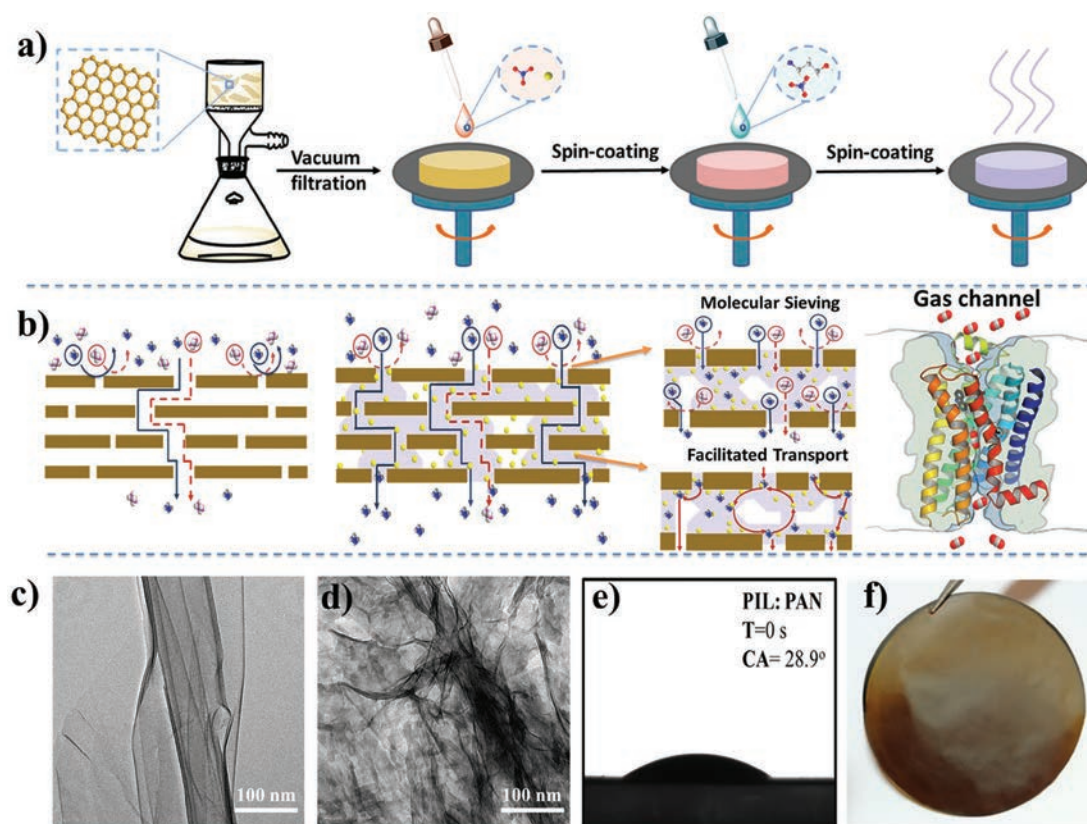


**Figure 1.** a) Fabrication process of the Ag/IL-GO membrane through three steps: vacuum-assisted self-assembly of GO nanosheets, the spin-coating of  $\text{AgNO}_3$  aqueous, and the spin-coating of IL to modify the 2D nanochannels. b) Dual transport mechanism of molecular sieving and carrier-facilitated transport by mimicking biological protein nanochannels. c) TEM image of pristine GO nanosheets. d) TEM image of Ag/IL-GO composite. e) Contact angle between the GO membrane and IL (PAN). f) Photograph of Ag/IL-GO membrane without PVDF support, making a free-standing membrane: the membrane thickness is about 10  $\mu\text{m}$  and IL content is about 18 wt%.

fabrication of GO membrane by vacuum-assisted filtration of single-layered GO nanosheet suspension on commercially available polyvinylidene fluoride (PVDF) support; fixation of silver carrier between the 2D nanochannels of GO membrane by spin-coating of AgNO<sub>3</sub> aqueous solution (Ag/GO); impregnation of IL into the 2D nanochannels of Ag/GO by spin-coating (Ag/IL-GO). Within the library of ILs, two different ILs (3-propanolammonium nitrate and 1-ethylimidazolium nitrate denoted as PAN and EIMN, respectively) are selected to highlight their structural effects on the separation performances (Figure S3, Supporting Information). The PAN and EIMN belong to protic ionic liquids, and have attributes such as high carrier (AgNO<sub>3</sub>) solubility, unique ability to stimulate activity of AgNO<sub>3</sub>, and typical protic acidic property, thus favoring for obtaining high ethylene/ethane separation performances with long-term stability.<sup>[6,7]</sup> Moreover, they are featured by reduced environmental impacts, such as low toxicity and high biodegradability, and their straightforward preparation reduces or eliminates additional work-up stages, such as solvent separation and ion-exchange reactions, which makes them much less expensive than other ILs. After the fixation of silver carrier and impregnation of IL, the Ag/IL-GO membranes are endowed with dual transport mechanisms of molecular sieving and carrier-facilitated transport (Figure 1b and Figure S4, Supporting Information). On the one hand, numerous in-plane slit-like nanopores (nano-wrinkles) within membrane are generated and tailored, where ethylene molecule is allowed to permeate while ethane is rejected, endowing the membrane with distinct molecular sieving mechanism. On the other hand, the carrier in the IL-GO environment exhibits high efficiency and facilitates the ethylene transport significantly within plane-to-plane 2D nanochannels. The content of IL can effectively manipulate the membrane separation performances. With IL content increasing, the 2D nanochannels vary from partial impregnation of IL to complete impregnation of IL, accompanied with that the molecular sieving first increases and then decreases, while the carrier-facilitated transport increases monotonously.

For the GO membranes, gas transport is strongly dependent on the size and stacking configuration of the GO nanosheets.<sup>[24]</sup> The relatively smaller size of GO nanosheets will produce a membrane with abundant slit-like nanopores.<sup>[25,26]</sup> Considering the large molecular kinetic diameters of ethylene (0.416 nm) and ethane (0.443 nm), the smaller size of GO nanosheets is favorable for obtaining the desired permeances. As observed by the transmission electron microscope (TEM, Figure 1c), the ultrathin and almost transparent GO nanosheets with lateral sizes of about 0.5–1 μm are utilized in this study, where some nanoscale wrinkles indicate the flexibility of GO nanosheets. The atomic force microscopy (AFM) images further confirm that the thickness of GO nanosheets is ≈1.1 nm, which indicates their single-layered structure (Figure S5, Supporting Information). The crystallinity of the GO nanosheets is revealed by the X-ray diffraction (XRD) measurement, which shows the characteristic (001) peak of GO at  $2\theta = 10.7^\circ$  (Figure S6, Supporting Information). Figure 1d shows the TEM image of Ag/IL-GO composite, where the nanosized shadows are the discontinuous IL nanodomains, indicative of IL attachment to specific sites on GO. Due to the interactions between GO nanosheet and IL/carrier, more wrinkles generate. The IL-GO

contact angles and the quick impregnation of IL within the GO nanochannels are presented in Figure 1e and Figure S7 in the Supporting Information. The good wettability between GO membrane and IL suggests the homogenous trapping of IL within the 2D nanochannels of GO by positive capillary force, and stable Ag/IL-GO membranes are easily fabricated. Figure 1f shows a typical digital photo of a 10 μm thick free-standing Ag/IL-GO membrane, which reveals sufficient mechanical robustness.

## 2.2. Membrane Structure and Composition Characterization

The microstructures of Ag/IL-GO membranes are effectively tailored by IL contents. Top-view scanning electron microscope (SEM) image of GO membrane shows a dense surface with some wrinkles and no visible defects (Figure 2a), while the cross-section image shows a well-packed 2D lamellar structure with a thickness of 2 μm (Figure 2b). After decorated with carrier and IL, the Ag/IL-GO membranes exhibit a distinctive appearance, where the GO nano-wrinkles and IL nanodomains are arranged in an alternating manner originated from the interactions between GO nanosheets and IL/carrier, which is in line with the above TEM observation (Figure 2c). With the increase of IL content, the GO nano-wrinkles and IL nanodomains vary obviously due to the stronger interactions, which means the size of nano-wrinkles can be easily manipulated (Figure S8a,b, Supporting Information). Moreover, these generated and enlarged nano-wrinkles can act as entrances for the gas penetrating into the 2D channels. As suggested by the cross-section images, the IL is impregnated into the GO layers successfully, and with the IL content increasing, the lamellar structure gradually becomes obscure, and the membrane thickness increases, e.g., 2.4 μm for IL content of 18 wt%, 3.0 μm for IL content of 33 wt%, and 4.0 μm for IL content of 52 wt%, respectively (Figure 2d and Figure S8c,d, Supporting Information). The membrane thickness is determined by the average value of experimental data at ten different locations on each sample (Figure S9, Supporting Information). The lamellar structure disappears completely when IL content reaches up to 52 wt%, which indicates all the 2D nanochannels are full of IL. Notably, the thickness of resulting membranes is much thinner than previously reported ethylene/ethane separation membranes (50–150 μm).<sup>[4,5]</sup> 3D surface AFM analysis of the membranes is conducted to further observe the surface morphology and roughness of the membranes (Figure 2e,f). Consistent with the result of SEM observations, the roughness of Ag/IL-GO membranes is slightly higher than that of pristine GO membrane and further increases with more IL impregnation (Figure S8e,f, Supporting Information). The elements of C, N, O, Ag are uniformly distributed as shown in the energy dispersive X-ray spectroscopy (EDS) mapping images (Figure S10, Supporting Information). The chemical compositions of the Ag/IL-GO membranes are confirmed by X-ray photoelectron spectroscopy (XPS, Figure S11, Supporting Information), which provides further evidence that the membrane is fabricated successfully as designed. The sizes of 2D nanochannels of Ag/IL-GO membranes are also measured by XRD.<sup>[27]</sup> Ag/IL-GO membranes exhibit broader and lower intensity peaks compared with pristine GO membrane, which is due

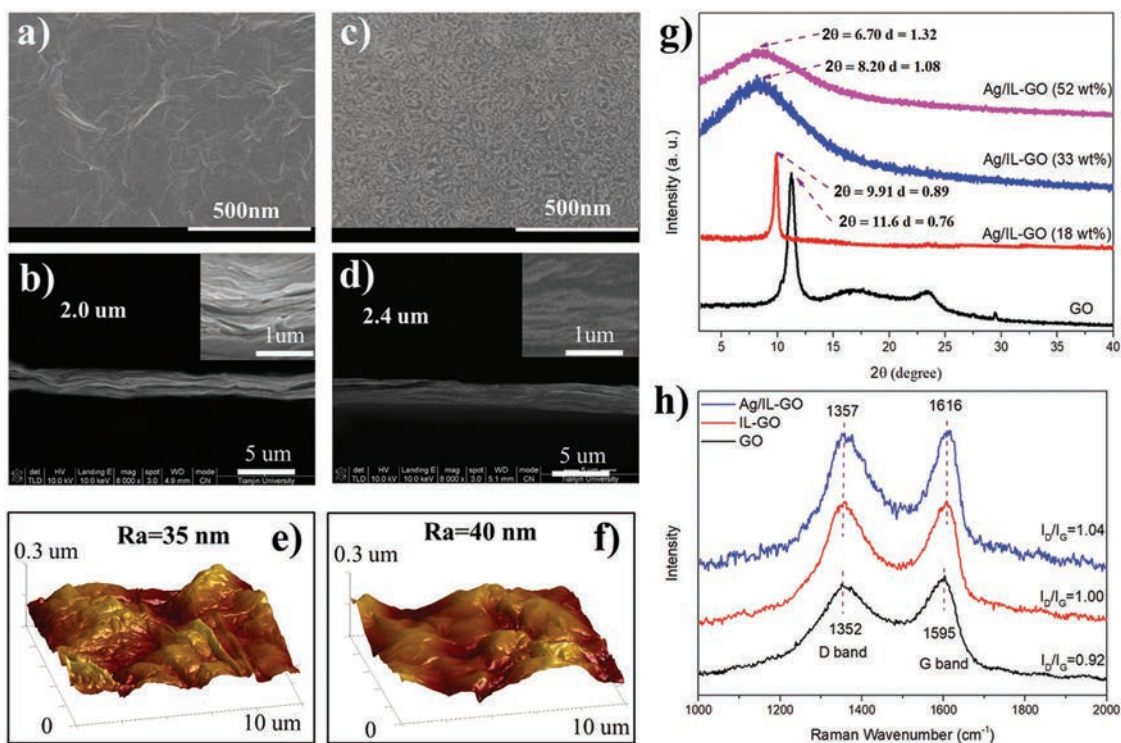


**Figure 2.** The structure of the Ag/IL-GO membranes taking EIMN for example. a, b) FE-SEM surface and cross-section images of GO membrane. c, d) FE-SEM surface and cross-section images of Ag/IL-GO membrane with the IL content of 18 wt%. e, f) 3D surface AFM images of GO and Ag/IL-GO membranes.  $R_a$  is average roughness. g) Analysis for the average interlayer height of 2D channels in membranes by XRD spectra in nm. h) Raman spectra of GO, IL-GO, and Ag/IL-GO membranes.

to the interactions within membranes altering the stacking of GO nanosheets. The interlayer spacing of pristine GO sheet is 0.76 nm as indicated by XRD (Figure 2g); after fixation of carrier and impregnation of IL with different contents, the interlayer spacing of the membranes is enlarged to 0.89, 1.08, and 1.32 nm for 18, 33, and 52 wt% IL, respectively. Considering the GO thickness of 0.35 nm, the size of 2D nanochannels is derived as: 0.41, 0.54, 0.73, and 0.97 nm, respectively.

Furthermore, the noncovalent interactions between the GO nanosheets and IL/carrier within Ag/IL-GO membranes, including cation–anion electrostatic interaction, hydrogen-bonding interaction,  $\pi$ – $\pi$  stacking interaction (Figure S12 (EIMN) and Figure S13 (PAN), Supporting Information), are characterized by Raman and attenuated total reflectance-Fourier transform infrared spectroscopy (ATR-FTIR).<sup>[26,28]</sup> The Raman spectra of Ag/IL-GO membrane show the D and G bands resulting from graphitic  $sp^2$  zone and typical oxidized  $sp^3$  zones occur at 1352 and 1595  $cm^{-1}$ , as shown in Figure 2h and Figure S14 in the Supporting Information. In contrast with pristine GO, the increase of  $I_D/I_G$  of IL-GO and Ag/IL-GO indicates that the interactions of GO with IL/carrier increase the atomic lattice defects and disordered degree of GO nanosheets. Compared with PAN IL (Figure S15, Supporting Information), the D and G bands of Ag/IL-GO prepared with EIMN exhibit slight shifts, which is probably due to the addition of  $\pi$ – $\pi$  stacking interaction between imidazolium groups and the aromatic rings of the GO sheets. The ATR-FTIR spectrum of GO membrane exhibits typical peaks of oxygen-containing

functional groups (Figure 3a and Figure S16, Supporting Information), such as the peaks in the range of 3200–3400  $cm^{-1}$  ( $\nu(O-H)$  from alcohol or carboxylic acid), 1731  $cm^{-1}$  ( $\nu(C=O)$  from carbonyl and carboxyl groups). As for the pure EIMN IL, the peaks at 3135  $cm^{-1}$  ( $\nu(N-H)$ ) are derived from the IL cation, while the peak at 1314  $cm^{-1}$  ( $\nu(N=O)$ ) is associated with IL anion.<sup>[7,21]</sup> After impregnation of IL within GO layer, the C=O stretching vibration for IL-GO shifts from 1731 to 1742  $cm^{-1}$ , revealing a possible electrostatic interaction between IL cation and  $COO^-$  of the GO sheets. The interaction of IL cation and GO weakens the cation–anion electrostatic interaction of IL, which results in a blueshift of IL anion (from 1314 to 1319  $cm^{-1}$ ). The blueshifts of N-H stretching vibrations in the IL cation suggest the hydrogen-bonding reconstruction between GO and IL.<sup>[29]</sup> Compared with IL-GO, the C=O peak in Ag/IL-GO spectrum shows a redshift, indicating newly formed carrier–GO interactions. The carrier competes with IL for the coordination with GO sheets and somewhat weakens the GO–IL interactions, which is indicative of the redshifts of N=O and N-H stretching vibrations. The similar phenomena are also observed in the ATR-FTIR spectra of membranes based on the PAN (Figure S16, Supporting Information).

### 2.3. Molecular Dynamics (MD) Simulation

The results of MD simulations further reconfirm that the interactions between the GO nanosheets and IL/carrier result in

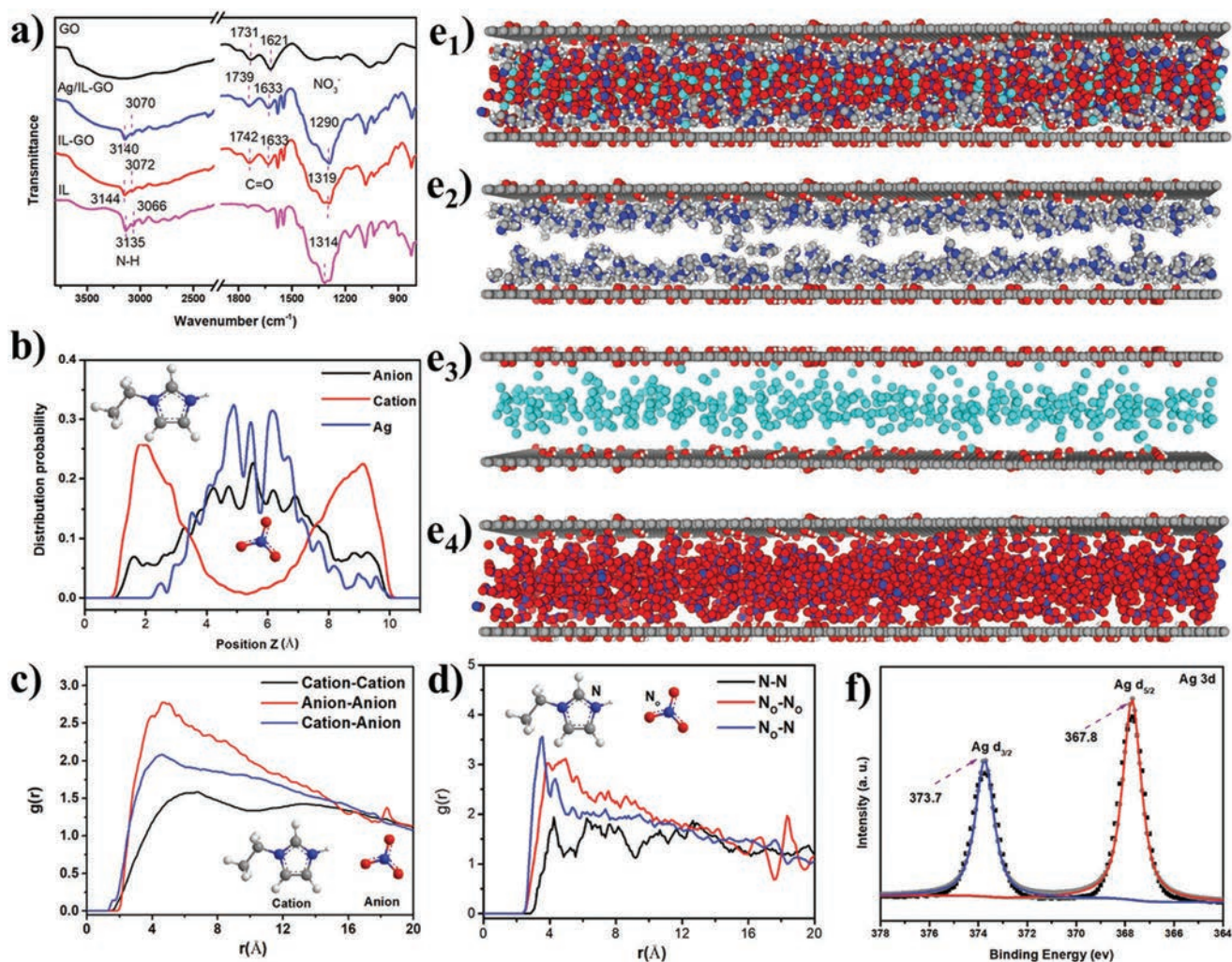


**Figure 3.** The noncovalent interactions within Ag/IL-GO membranes, IL is EIMN: a) ATR-FTIR spectra of IL, GO, IL-GO, and Ag/IL-GO membranes. b) Spatial distribution of the IL cation,  $\text{NO}_3^-$ , and silver ion along the width direction of the GO nanochannel. c) Radial distribution functions of cation–cation, cation–anion, and anion–anion structures in GO nanochannel. d) Radial distribution functions of atom–atom pair correlations. e<sub>1</sub>–e<sub>4</sub>) Nanostructure of carrier and IL within the GO nanosheets, where the colors of gray, white, red, blue, and Tiffany blue represent the atoms of carbon, hydrogen, oxygen, nitrogen, and silver, respectively, e<sub>1</sub>) IL and carrier, e<sub>2</sub>) cation of IL, e<sub>3</sub>) silver cation, e<sub>4</sub>)  $\text{NO}_3^-$  anion derived from both IL and silver salt. f) Verification of high carrier activity by XPS spectrum.

the layered nanostructures of fixed carrier and impregnated IL, which promotes carrier efficiency for transporting ethylene molecules. As clearly seen from Figure 3b, two peaks of IL cation are located at near the GO walls, while a broad peak of  $\text{NO}_3^-$  mainly segregates to the center of 2D nanochannels, which is attributable to the stronger IL cation–GO interactions. The noncovalent GO–cation interactions and cation–cation solvophobic force the cation to cluster together into apolar domains along the GO walls; the electrostatic and hydrogen bonding interactions of cation– $\text{NO}_3^-$  lead to the formation of polar domains (Figure 3c–e). Silver ions mainly place themselves in the polar domains and continuous silver ion distribution is obtained, contributing to the fast and selective ethylene molecule transport (Figure 3e). Meanwhile, some silver ions are also fixed on the GO walls, which lead to the hopping transport of ethylene molecules along GO interfacial pathways. Moreover, the high carrier efficiency is further verified by  $\text{Ag}_{3d}$

XPS spectrum, which is highly sensitive to carrier efficiency (Figure 3f). Compared with  $\text{Ag } 3d_{5/2}$  spectrum of pure  $\text{AgNO}_3$  (371.7 eV) in the previous report, the binding energy of silver salt in the Ag/IL-GO membrane significantly decreases to 367.8 eV, which reveals their enhanced charge density in IL-GO environment and strong ability to transport ethylene molecules, thus realizing highly efficient carrier-facilitated transport.<sup>[30]</sup>

#### 2.4. Gas Separation Performance and Dual Transport Mechanisms

The Ag/IL-GO membranes exhibit molecular sieving mechanism, which is distinctly demonstrated by their separation performances for pure  $\text{H}_2$ ,  $\text{CO}_2$ ,  $\text{N}_2$ , and  $\text{CH}_4$  gases (molecular kinetic diameters of 0.289, 0.330, 0.364, and 0.380 nm, respectively), where the carrier-facilitated transport has been excluded

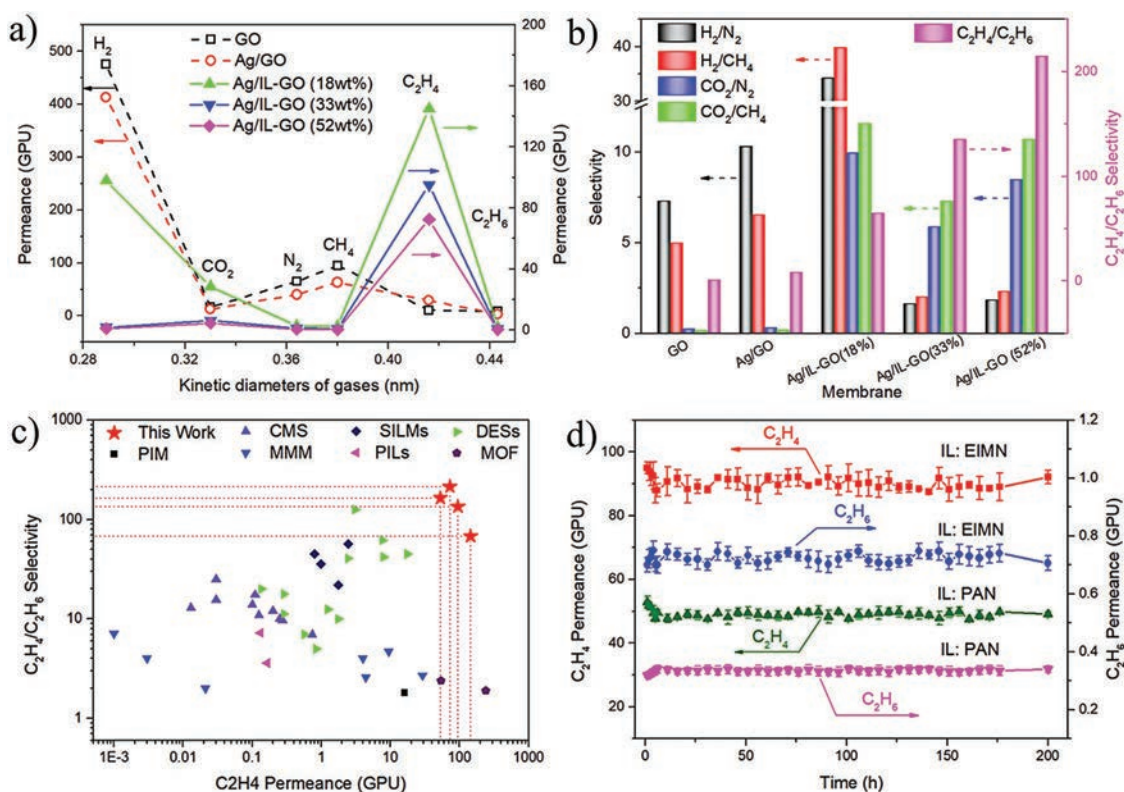


**Figure 4.** The gas transport properties of Ag/IL-GO membranes taking EIMN, e.g. a) The gas permeances of pure gases ( $H_2$ ,  $CO_2$ ,  $N_2$ , and  $CH_4$ ) and mixed gases ( $C_2H_4/C_2H_6$  50 vol%/50 vol%) through membranes based on EIMN. b) The corresponding ideal gas selectivity of  $H_2/N_2$ ,  $H_2/CH_4$ ,  $CO_2/N_2$ ,  $CO_2/CH_4$ , and mixed gas selectivity of  $C_2H_4/C_2H_6$ . c) Comparison of  $C_2H_4/C_2H_6$  separation performance with different types of membranes reported during the period 2010–2019. d) Long-term stability for  $C_2H_4/C_2H_6$  separation of Ag/IL-GO membranes with IL content of 33 wt%.

due to the absence of coordination between carrier with these gases.<sup>[31]</sup> As seen from **Figure 4a**, the pristine GO membrane exhibits the highest  $H_2$  permeance, and the gas permeances of  $CO_2$ ,  $N_2$ , and  $CH_4$  diverge their kinetic diameters, which is also observed in previous reports.<sup>[10]</sup> With the increase of impregnated IL content, the membranes vary from partial impregnation of IL to complete impregnation of IL, and the sizes of nanochannels and nanopores increase (Figure S17, Supporting Information). For the Ag/IL-GO (18 wt%) membranes, the permeances of  $H_2$ ,  $N_2$ , and  $CH_4$  decrease significantly, which is ascribed to the significant decrease of the effective size of nanochannels and nanopores. On the one hand, the impregnation of IL enlarges the sizes of nanochannels and nanopores; on the other hand, it blocks the nanochannels and nanopores. Due to the relatively high IL content, the blocking effect becomes major factor, and thus the effective size of nanochannels and nanopores decrease with the increase of IL content. For the Ag/IL-GO (33 wt%) and Ag/IL-GO (52 wt%) membranes, the nanochannels and nanopores are filled with IL completely, the permeances of  $H_2$ ,  $N_2$ , and  $CH_4$  are very low and remain almost constant. In contrast, the  $CO_2$  permeance increases for the Ag/IL-GO (18 wt%) membrane, and then decreases for the Ag/IL-GO (33 wt%) and Ag/IL-GO (52 wt%) membranes. The impregnated IL exhibits high solubility of  $CO_2$ , favoring for the increase of  $CO_2$  permeances (18 wt%). However, when the nanochannels and nanopores are completely filled with IL (33 and 52 wt%), the membrane thicknesses increase sharply

and the transport resistance increases significantly, thus resulting in the decrease of  $CO_2$  permeance. Moreover, the solubility and diffusivity of  $H_2$ ,  $N_2$ ,  $CH_4$ , and  $CO_2$  have been measured in order to gain deep insight of gas transport through Ag/IL-GO membranes (Table S1, Supporting Information). As seen from Table S1 in the Supporting Information, the solubilities of  $H_2$ ,  $N_2$ , and  $CH_4$  are very low, and their gas permeances are mainly manipulated by the diffusivity, while the  $CO_2$  permeance is mainly controlled by its solubility.

As seen from **Figure 4b**, for Ag/GO and Ag/IL-GO (18 wt%) membranes, the gas selectivities increase significantly. Especially, the Ag/IL-GO (18 wt%) membrane exhibits the highest selectivity for the four gas pairs. For example,  $H_2/N_2$  selectivity and  $H_2/CH_4$  selectivity reach up to 35 and 40, which verifies the molecular sieving property of our membranes. In general, molecular sieving of 2D membranes is primarily derived from either in-plane slit-like pores or plane-to-plane 2D nanochannels.<sup>[32]</sup> Particularly, many investigations have demonstrated that the slit-like pores play a critical role in determining the molecular sieving of membranes.<sup>[33]</sup> In our work, as suggested by the above XRD results, the spacings of 2D nanochannels are larger than all the gas kinetic diameters. Therefore, the molecular sieving of our membranes can be attributed to the in-plane slit-like pores (nanowrinkles). The decrease of nanopore size has more pronounced effect on the  $CH_4$  and  $N_2$  diffusivity than that of  $H_2$  due to their larger MD diameters, which contributes to the increase of  $H_2/N_2$  selectivity and  $H_2/CH_4$  selectivity at IL content of 18 wt%. For

the Ag/IL-GO (33 wt%) and Ag/IL-GO (52 wt%) membranes, the  $H_2/N_2$  and  $H_2/CH_4$  selectivities decrease sharply, which hints the full impregnation of IL within nanopores substantially blocks the diffusion of  $H_2$ ,  $N_2$ ,  $CH_4$ , weakening molecular sieving. However, the Ag/IL-GO membranes with impregnation of IL exhibit higher  $CO_2/N_2$  and  $CO_2/CH_4$  selectivity than that of GO and Ag/GO membranes. The Ag/IL-GO membrane (18 wt%) exhibits the highest selectivity due to its synergy of diffusivity selectivity and solubility selectivity. The gas selectivity data indicate the membrane is transferred from “diffusion-controlled” to “solubility-controlled” with the impregnated IL content increasing. As seen from Table S2 in the Supporting Information, the  $H_2/CH_4$  permeability selectivity is controlled by its diffusivity selectivity without IL or with low content IL (18 wt%), while the  $CO_2/CH_4$  selectivity is controlled by solubility selectivity with the high IL content (33 and 52 wt%).

In contrast, the Ag/IL-GO membranes exhibit superior dual transport mechanisms for equal-molar  $C_2H_4/C_2H_6$  mixed gas separation. As also presented in Figure 4a,b, all the Ag/IL-GO membranes exhibit extremely high  $C_2H_4$  permeance and  $C_2H_4/C_2H_6$  selectivity arisen from the dual transport mechanisms. After the fixation of carrier and impregnation of IL, plenty of in-plane slit-like pores and ethylene-selective plane-to-plane nanochannels are constructed, which achieves the synergism of molecular sieving and carrier-facilitated transport. As expected, the  $C_2H_4$  permeance is remarkably enhanced by nearly 15 times, increasing from 10.7 GPU for pristine GO membrane to 145 GPU for the Ag/IL-GO (18 wt%) membrane. With the IL content increasing up to 33 and 52 wt%, both  $C_2H_4$  and  $C_2H_6$  permeances decrease due to the increased transport resistance accompanied with the visible increase of the membrane thickness. Fortunately, the decrease of  $C_2H_4$  permeance is much smaller than that of  $C_2H_6$ , which is ascribed to the enhanced carrier-facilitated transport with more impregnated IL within nanochannels. With more IL impregnation, more silver salt is activated and disassociated into silver ions, which facilitate the transport of ethylene molecules significantly (Figure S18, Supporting Information). As a result, the  $C_2H_4/C_2H_6$  selectivity reaches up to 215 with IL content of 52 wt%. The superhigh selectivity of 215 and high  $C_2H_4$  permeance of 72.5 GPU enable the possible application of the membrane for manufacturing polymer-grade ethylene through a highly energy-efficient approach. Moreover, the  $C_2H_4/C_2H_4$  separation performance of IL-GO membrane without silver salt carrier is also conducted as a control experiment, which verifies the remarkable enhancement of gas separation performance by the carrier-facilitated transport (Figure S19, Supporting Information). Furthermore, the effect of different IL structure on the separation performances is also investigated, which manifests the facile manipulation of membrane separation performance by changing impregnated IL (Figure S20, Supporting Information).<sup>[6,7]</sup> It is widely acknowledged that the carrier-facilitated transport and molecular sieving mainly affect the gas solubility and diffusion within the membrane, respectively. Therefore, the dual transport mechanisms are qualitatively described by gas thermodynamic solubility and kinetic diffusivity. As seen from Figure S21 in the Supporting Information, the Ag/IL-GO membranes with IL content of 18, 33, and 52 wt% exhibit about 25 times, 50 times, and 100 times higher solubility selectivity

than that of pristine GO membrane, confirming the carrier-facilitated transport within the Ag/IL-GO membranes. On the other hand, the diffusivity selectivity of Ag/IL-GO membranes is much superior to pristine GO membrane, especially for the Ag/IL-GO membrane (18 wt%), exhibiting three times higher diffusivity selectivity, which provides sufficient evidence for molecular sieving (Figure S21, Supporting Information).

The superior  $C_2H_4/C_2H_6$  separation performances of Ag/IL-GO membranes have been highlighted by comparing with recently reported membranes in terms of selectivity-permeance. As illustrated in Figure 4c, the Ag/IL-GO membranes show superior performances compared with polyimide membranes, carbon molecular sieve membranes, mixed matrix membranes, supported IL membranes, poly IL membranes, deep eutectic solvent membranes, and MOF membranes (Tables S3–S9, Supporting Information). The Ag/IL-GO membranes also exceed the 2013 upper-bound for polymeric membranes, and exhibit better performances than most of the membranes based on selectivity-permeability (Figure S22, Supporting Information). The thinner separation layer of our membranes also means a lower-cost membrane fabrication (Figure S22, Supporting Information). The unprecedented separation performances can be due to the elaborate design of membrane structure, which achieve dual transport mechanisms. An initial optimization of separation parameters, including transmembrane pressure, operating temperature, and the flow rate of sweep gas, is conducted to promote the separation process efficiency (Figures S23–S25, Supporting Information). The combinations of lower transmembrane pressure, lower operating temperature, and moderate sweep gas flow rate account for a more energy-efficient membrane separation process with higher  $C_2H_4/C_2H_6$  selectivity. Moreover, a continuous permeation of  $C_2H_4$  and  $C_2H_6$  is carried out for 200 h, the stable gas permeances and selectivity indicate that our membranes are mechanically robust and chemically stable (Figure 4d and Figure S26, Supporting Information).

### 3. Conclusion

In summary, we present, from inception to implementation, a highly permeable and selective Ag/IL-GO membrane fabricated by using silver ion and IL as ethylene transport carrier and decoration agents for the GO nanochannels. By adjusting the amount of impregnated IL and GO–IL/carrier interactions, the in-plane nano-wrinkles can be generated and further tailored for enhancing ethylene/ethane sieving property of GO membranes; meanwhile, the carriers fixed within 2D nanochannels exhibit high activity, thus greatly facilitating ethylene transport. Benefiting from dual transport mechanisms, the Ag/IL-GO exhibits superhigh ethylene/ethane selectively and high ethylene permeance, out-performing most of the state-of-art ethylene/ethane separation membranes. Furthermore, the membranes possess long-term stability, which renders great potential for industrial ethylene/ethane separations. Our methodology for incorporating dual transport mechanism driven by a biomimetic design, may open up a novel avenue to 2D nanochannel construction and will also shed light on the design of high-performance membranes for gas capture, ion sieving, and organic solvent separation.

## 4. Experimental Section

**Materials:** All gases with a minimum mole fraction of 99.9% were all provided by Tianjin Air Liquide Co., Ltd (China), including hydrogen (H<sub>2</sub>), carbon dioxide (CO<sub>2</sub>), nitrogen (N<sub>2</sub>), methane (CH<sub>4</sub>), ethylene (C<sub>2</sub>H<sub>4</sub>), and ethane (C<sub>2</sub>H<sub>6</sub>). Natural flake graphite (60 μm) was purchased from Qingdao Tianhe Graphite (China). Sulfuric acid (H<sub>2</sub>SO<sub>4</sub>, 98 wt%), phosphoric acid (H<sub>3</sub>PO<sub>4</sub>, 85 wt%), and hydrochloric acid (HCl, 36–38 wt%) were purchased from Tianjin Fengchuan Chemical Reagent Technologies Co., Ltd. (China) and used as received. Potassium permanganate (KMnO<sub>4</sub>, 99.8 wt%) and hydrogen peroxide (H<sub>2</sub>O<sub>2</sub>, 30 wt%) were supplied by Shanghai Aladdin Biochem Technology Co., Ltd. (China). 1-ethylimidazole (98 wt%) and 1,3-propanolamine (97 wt%) were obtained from Tianjin Guangfu Technology Development Co. Ltd. (China) and redistilled under vacuum before use. Methanol was purchased from Tianjin Kermel Chemical Reagent Co., Ltd. (China). The hydrophilic PVDF membrane was selected as support and obtained from Haining Zhongli Filtering Equipment Co., Ltd. (China), which has the average thickness of 100 μm, the porosity of 70%, and a nominal pore size of 0.1 μm.

**Membrane Fabrication:** The preparation of Ag/IL-GO membrane is described in detail as follows: 1) Fabrication of GO membrane by vacuum-assisted filtration method, a certain amount GO powder was dispersed into water under ultrasonic treatment and stirred for 5 h to obtain GO nanosheet suspension (0.05 mg mL<sup>-1</sup>) and then stable dispersed GO aqueous solution was filtered through PVDF support and dried in a fume hood at room temperature for 24 h; 2) fixation of silver carrier between the 2D nanochannels of GO membrane by spin-coating, the GO was set on a spin coater (WS-650-23B, Laurell Technologies Co., Ltd, USA), and spun with 0.5 mL AgNO<sub>3</sub> aqueous solution (0.05 mol L<sup>-1</sup>) for 10 s at 500 rpm, followed by drying at room temperature for 48 h to obtain Ag/GO membrane; 3) impregnation of IL into the 2D nanochannels of GO by spin-coating, the Ag/GO membrane was placed on a spin coater and spun at 1000 rpm, the desired amount of IL/water mixture (95 vol%:5 vol%) was dropped onto the membrane surface and kept on spinning for 15 s, the spin-coating was also repeated for several times (1–5) to accomplish the fabrication of Ag/IL-GO membranes. For the membrane fabrication, all the membranes contained the same amount of GO (≈2.5 mg) and silver salt (≈2.0 mg), while the amount of IL varied at 18, 33, and 52 wt%. The IL weight percent was calculated by the equation:  $M_{IL}/(M_{IL} + M_{GO})$ . Benefiting from very large positive capillary force, the AgNO<sub>3</sub> aqueous solution and IL were easily impregnated with 2D nanochannels of membranes. Moreover, the spin-coating distributed AgNO<sub>3</sub> aqueous solution or IL homogeneously on the surface of GO or Ag/GO membrane, respectively, which created prerequisite for the uniform impregnation of AgNO<sub>3</sub> aqueous solution or IL. Meanwhile, the multiple runs of spin-coating also favored for the uniform distribution of carrier and IL.

**Characterizations:** The morphology and dimensions of GO nanosheet and Ag/IL-GO composite were observed using TEM (JEM-1011, JEOL). The membrane morphology, including freeze-fractured cross-section and surface, was examined by a field-emission SEM (FE-SEM, Phenom G2) after the samples were sputter-coated with gold-palladium alloy. The chemical composition of the membrane was mapped using EDS configured with FE-SEM. The GO nanosheets and the roughness of the membranes were investigated by AFM (Bruker MultiMode 8) in tapping mode. The compatibility between IL and GO was evaluated by a contact angle goniometer (Powereach JC2000C), which was performed at room temperature for at least three measurements on each sample. The crystallinity of the membranes and the d-spacing of stacked GO nanosheets were analyzed using Cu-Kα XRD (PANalytical Empyrean) with the 2θ from 5° to 50° at the speed of 5° min<sup>-1</sup>. The d-spacing was calculated based on Bragg's law:  $2d\sin\theta = n\lambda$ . The information about chemical composition and bonding chemistry for the surface layer of the membrane was characterized by XPS (Escalab 250Xi) with a monochromatic aluminum Kα X-ray source, which was operated within the range from 0 to 1400 eV with 1 eV resolution. The interactions within the membrane were determined by ATR-FTIR (Perkin Elmer, Spectrum 100)

with a resolution of 4 cm<sup>-1</sup> in the range of 4000–400 cm<sup>-1</sup>. The structural properties, mainly including the G and D bands, were characterized by Raman spectroscopy (Raman, JY Horiba) equipped with a charge coupled device (CCD) detector, and a He-Ne (633 nm) laser for excitation. Finally, it should be noted that the selective layer was peeled off from the PVDF support for the SEM and XRD characterizations in order to exclude the interference of PVDF support.

**Permeation:** The separation performances of GO, Ag/GO, Ag/GO-IL membranes were evaluated by a stainless steel membrane cell for the gas with different kinetic diameters, including H<sub>2</sub> (0.289 nm), CO<sub>2</sub> (0.330 nm), N<sub>2</sub> (0.364 nm), CH<sub>4</sub> (0.380 nm), and mixed gas (ethylene (0.416 nm)/ethane (0.444 nm) 50:50 Vol%) (Supporting Information). The pure or mixed gas flowing through the feed side was adjusted by the mass flow controller. The feed gas pressure was regulated by a micrometer valve and measured by a pressure sensor. The flux and composition of permeated gas were measured by gas mass flowmeter and online gas chromatography, respectively. Three parallel experiments were carried out to obtain the average value as the gas permeance or permeability, which is described by Equations (1) and (2)

$$P_i = \frac{L_i}{A \cdot \Delta P_i} \quad (1)$$

$$P_{yi} = \frac{L_i \delta}{A \cdot \Delta P_i} \quad (2)$$

where  $P_i$  is the gas permeance through the composite membrane of the component  $i$  (GPU, 1 GPU =  $1 \times 10^{-6}$  cm<sup>3</sup> cm<sup>-2</sup> S<sup>-1</sup> cmHg<sup>-1</sup>),  $P_{yi}$  is the gas permeability through the composite membrane of the component  $i$  (Barrer, 1 Barrer =  $1 \times 10^{-10}$  cm<sup>3</sup> cm cm<sup>-2</sup> S<sup>-1</sup> cmHg<sup>-1</sup>),  $L_i$  is the permeation flux of component  $i$  through the membrane (cm<sup>3</sup> S<sup>-1</sup>);  $\Delta P_i$  is the pressure difference between the feed and permeate side (cmHg);  $A$  is the effective membrane area (3.14 cm<sup>2</sup> in this study); and  $\delta$  is the membrane thickness (cm).

The permeability could be further represented as the product of thermodynamic adsorption coefficient ( $S$ ), and kinetic effective diffusion coefficient ( $D$ )

$$P_i = S_i \cdot D_i \quad (3)$$

The gas solubility coefficient was determined by the gas adsorption capacity ( $n_i$ ), and then the effective diffusion coefficient was derived from the division of gas permeability by gas adsorption coefficient (Supporting Information). The gas selectivity ( $\alpha_{ij}$ ) was obtained by dividing the permeability of the more permeable species  $i$  to the permeability of the less permeable species  $j$  for the case where the downstream pressure was negligible relative to the upstream feed pressure, which was further expressed as the product of the diffusivity selectivity and the solubility selectivity

$$\alpha_{ij} = \frac{P_i}{P_j} = \frac{S_i}{S_j} \cdot \frac{D_i}{D_j} \quad (4)$$

**Theoretical Simulation:** The nanostructure of IL and carrier within the GO nanochannels was investigated by MD simulations using large scale atomic/molecular massively parallel simulator (LAMMPS) package (Supporting Information). The optimized potentials for liquid simulations-all atoms force field was used for GO structure simulation, while the AMBER force field was used for the IL EIMN. The 2D nanochannel was consisted of two parallel GO sheets with dimensions of 15.1 nm × 4.3 nm, where the periodic boundary conditions were only applied in the lateral directions. The size of the 2D nanochannel was fixed at 1.08 nm according to the XRD results. The system was equilibrated at 300 K for 3 ns with box sizes of 42.6 × 152.5 × 11 Å<sup>3</sup>. Subsequently, another run of 5 ns was carried out to produce data for analyzing the IL structures.

## Supporting Information

Supporting Information is available from the Wiley Online Library or from the author.



## Acknowledgements

The authors greatly appreciate the support from the Natural Sciences and Engineering Research Council of Canada (NSERC), University of Waterloo, National Natural Science Foundation of China (21838008), and National Key R&D Program of China (no. 2017B0602702).

## Conflict of Interest

The authors declare no conflict of interest.

## Keywords

bioinspired membranes, carrier-facilitated transport, graphene oxide, molecular separation, molecular sieving

Received: June 30, 2019

Revised: September 5, 2019

Published online: October 9, 2019

- [1] a) L. Li, R.-B. Lin, R. Krishna, H. Li, S. Xiang, H. Wu, J. Li, W. Zhou, B. Chen, *Science* **2018**, *362*, 443; b) R.-B. Lin, L. Li, H.-L. Zhou, H. Wu, C. He, S. Li, R. Krishna, J. Li, W. Zhou, B. Chen, *Nat. Mater.* **2018**, *17*, 1128.
- [2] a) B. Li, Y. Zhang, R. Krishna, K. Yao, Y. Han, Z. Wu, D. Ma, Z. Shi, T. Pham, B. Space, J. Liu, P. K. Thallapally, J. Liu, M. Chrzanowski, S. Ma, *J. Am. Chem. Soc.* **2014**, *136*, 8654; b) S. Chu, Y. Cui, N. Liu, *Nat. Mater.* **2017**, *16*, 16.
- [3] a) Z. Qiao, S. Zhao, M. Sheng, J. Wang, S. Wang, Z. Wang, C. Zhong, M. D. Guiver, *Nat. Mater.* **2019**, *18*, 163; b) Y. Belmabkhout, P. M. Bhatt, K. Adil, R. S. Pillai, A. Cadiou, A. Shkurenko, G. Maurin, G. Liu, W. J. Koros, M. Eddaoudi, *Nat. Energy* **2018**, *3*, 1059.
- [4] J. E. Bachman, Z. P. Smith, T. Li, T. Xu, J. R. Long, *Nat. Mater.* **2016**, *15*, 845.
- [5] a) J. Liu, Y. Xiao, T.-S. Chung, *J. Mater. Chem. A* **2017**, *5*, 4583; b) L. C. Tomé, D. Mecerreyes, C. S. R. Freire, L. P. N. Rebelo, I. M. Marrucho, *J. Mater. Chem. A* **2014**, *2*, 5631; c) B. Jiang, H. Dou, B. Wang, Y. Sun, Z. Huang, H. Bi, L. Zhang, H. Yang, *ACS Sustainable Chem. Eng.* **2017**, *5*, 6873.
- [6] a) M. J. Lee, H. T. Kwon, H.-K. Jeong, *Angew. Chem.* **2018**, *130*, 162; b) B. Jiang, H. Dou, L. Zhang, B. Wang, Y. Sun, H. Yang, Z. Huang, H. Bi, *J. Membr. Sci.* **2017**, *536*, 123; c) Y. Liu, Z. Chen, G. Liu, Y. Belmabkhout, K. Adil, M. Eddaoudi, W. Koros, *Adv. Mater.* **2019**, *31*, 1807513.
- [7] H. Dou, B. Jiang, X. Xiao, M. Xu, X. Tantai, B. Wang, Y. Sun, L. Zhang, *ACS Appl. Mater. Interfaces* **2018**, *10*, 13963.
- [8] M. Rungta, C. Zhang, W. J. Koros, L. Xu, *AIChE J.* **2013**, *59*, 3475.
- [9] H. B. Park, J. Kamcev, L. M. Robeson, M. Elimelech, B. D. Freeman, *Science* **2017**, *356*, eaab0530.
- [10] a) H. Zarrin, J. Fu, G. Jiang, S. Yoo, J. Lenos, M. Fowler, Z. Chen, *ACS Nano* **2015**, *9*, 2028; b) J. Liu, N. Wang, L.-J. Yu, A. Karton, W. Li, W. Zhang, F. Guo, L. Hou, Q. Cheng, L. Jiang, D. A. Weitz, Y. Zhao, *Nat. Commun.* **2017**, *8*, 2011; c) J. Shen, G. Liu, Y. Ji, Q. Liu, L. Cheng, K. Guan, M. Zhang, G. Liu, J. Xiong, J. Yang, W. Jin, *Adv. Funct. Mater.* **2018**, *28*, 1801511; d) H. Huang, Z. Song, N. Wei, L. Shi, Y. Mao, Y. Ying, L. Sun, Z. Xu, X. Peng, *Nat. Commun.* **2013**, *4*, 2979; e) L. Chen, G. Shi, J. Shen, B. Peng, B. Zhang, Y. Wang, F. Bian, J. Wang, D. Li, Z. Qian, G. Xu, G. Liu, J. Zeng, L. Zhang, Y. Yang, G. Zhou, M. Wu, W. Jin, J. Li, H. Fang, *Nature* **2017**, *550*, 380.
- [11] a) H. Li, Z. Song, X. Zhang, Y. Huang, S. Li, Y. Mao, H. J. Ploehn, Y. Bao, M. Yu, *Science* **2013**, *342*, 95; b) L. Huang, J. Chen, T. Gao, M. Zhang, Y. Li, L. Dai, L. Qu, G. Shi, *Adv. Mater.* **2016**, *28*, 8669; c) Y. Long, K. Wang, G. Xiang, K. Song, G. Zhou, X. Wang, *Adv. Mater.* **2017**, *29*, 1606093; d) K. H. Thebo, X. Qian, Q. Zhang, L. Chen, H.-M. Cheng, W. Ren, *Nat. Commun.* **2018**, *9*, 1486; e) K. Huang, G. Liu, J. Shen, Z. Chu, H. Zhou, X. Gu, W. Jin, N. Xu, *Adv. Funct. Mater.* **2015**, *25*, 5809.
- [12] a) J. Yang, D. Gong, G. Li, G. Zeng, Q. Wang, Y. Zhang, G. Liu, P. Wu, E. Vovk, Z. Peng, X. Zhou, Y. Yang, Z. Liu, Y. Sun, *Adv. Mater.* **2018**, *30*, 1705775; b) F. Zhou, H. N. Tien, W. L. Xu, J.-T. Chen, Q. Liu, E. Hicks, M. Fathizadeh, S. Li, M. Yu, *Nat. Commun.* **2017**, *8*, 2107; c) W.-S. Hung, C.-H. Tsou, M. De Guzman, Q.-F. An, Y.-L. Liu, Y.-M. Zhang, C.-C. Hu, K.-R. Lee, J.-Y. Lai, *Chem. Mater.* **2014**, *26*, 2983; d) S. Wang, Y. Xie, G. He, Q. Xin, J. Zhang, L. Yang, Y. Li, H. Wu, Y. Zhang, M. D. Guiver, Z. Jiang, *Angew. Chem., Int. Ed.* **2017**, *56*, 14246.
- [13] a) N. C. Su, D. T. Sun, C. M. Beavers, D. K. Britt, W. L. Queen, J. J. Urban, *Energy Environ. Sci.* **2016**, *9*, 922; b) L. Xiang, L. Sheng, C. Wang, L. Zhang, Y. Pan, Y. Li, *Adv. Mater.* **2017**, *29*, 1606999.
- [14] a) G. Xie, P. Li, Z. Zhao, X.-Y. Kong, Z. Zhang, K. Xiao, H. Wang, L. Wen, L. Jiang, *Angew. Chem.* **2018**, *130*, 16950; b) N. Uehlein, C. Lovisollo, F. Siefert, R. Kaldenhoff, *Nature* **2003**, *425*, 734; c) J. S. Hub, B. L. de Groot, *Proc. Natl. Acad. Sci. U. S. A.* **2008**, *105*, 1198.
- [15] B. Wu, E. Beitz, *Cell. Mol. Life Sci.* **2007**, *64*, 2413.
- [16] S. Wang, Y. Wu, N. Zhang, G. He, Q. Xin, X. Wu, H. Wu, X. Cao, M. D. Guiver, Z. Jiang, *Energy Environ. Sci.* **2016**, *9*, 3107.
- [17] a) C. S. Lee, M.-K. Choi, Y. Y. Hwang, H. Kim, M. K. Kim, Y. J. Lee, *Adv. Mater.* **2018**, *30*, 1705944; b) Y.-X. Shen, W. Song, D. R. Barden, T. Ren, C. Lang, H. Feroz, C. B. Henderson, P. O. Saboe, D. Tsai, H. Yan, P. J. Butler, G. C. Bazan, W. A. Phillip, R. J. Hickey, P. S. Cremer, H. Vashith, M. Kumar, *Nat. Commun.* **2018**, *9*, 2294.
- [18] a) Z. Zhang, L. Wen, L. Jiang, *Chem. Soc. Rev.* **2018**, *47*, 322; b) P. Agre, *Angew. Chem., Int. Ed.* **2004**, *43*, 4278.
- [19] a) I. S. Chae, S. W. Kang, J. Y. Park, Y.-G. Lee, J. H. Lee, J. Won, Y. S. Kang, *Angew. Chem.* **2011**, *123*, 3038; b) M. G. Cowan, W. M. McDanel, H. H. Funke, Y. Kohno, D. L. Gin, R. D. Noble, *Angew. Chem.* **2015**, *127*, 5832; c) F. Pitsch, F. F. Krull, F. Agel, P. Schulz, P. Wasserscheid, T. Melin, M. Wessling, *Adv. Mater.* **2012**, *24*, 4306.
- [20] a) A. S. Amarasekara, *Chem. Rev.* **2016**, *116*, 6133; b) T. L. Greaves, C. J. Drummond, *Chem. Rev.* **2015**, *115*, 11379.
- [21] H. Dou, B. Jiang, X. Xiao, M. Xu, B. Wang, L. Hao, Y. Sun, L. Zhang, *J. Membr. Sci.* **2018**, *557*, 76.
- [22] a) H. Dou, B. Jiang, L. Zhang, M. Xu, Y. Sun, *J. Membr. Sci.* **2018**, *567*, 39; b) H. Dou, B. Jiang, M. Xu, J. Zhou, Y. Sun, L. Zhang, *Chem. Eng. Sci.* **2019**, *193*, 27; c) M. Watanabe, M. L. Thomas, S. Zhang, K. Ueno, T. Yasuda, K. Dokko, *Chem. Rev.* **2017**, *117*, 7190.
- [23] J. Chen, B. Yao, C. Li, G. Shi, *Carbon* **2013**, *64*, 225.
- [24] a) S. Cong, H. Li, X. Shen, J. Wang, J. Zhu, J. Liu, Y. Zhang, B. Van der Bruggen, *J. Mater. Chem. A* **2018**, *6*, 17854; b) Y. Zhao, C. Zhou, J. Wang, H. Liu, Y. Xu, J. W. Seo, J. Shen, C. Gao, B. Van der Bruggen, *J. Mater. Chem. A* **2018**, *6*, 18859.
- [25] Y. Zhang, Q. Shen, J. Hou, P. D. Sutrisna, V. Chen, *J. Mater. Chem. A* **2017**, *5*, 7732.
- [26] W. Fam, J. Mansouri, H. Li, J. Hou, V. Chen, *ACS Appl. Mater. Interfaces* **2018**, *10*, 7389.
- [27] W. Li, W. Wu, Z. Li, *ACS Nano* **2018**, *12*, 9309.
- [28] Y. Ban, Z. Li, Y. Li, Y. Peng, H. Jin, W. Jiao, A. Guo, P. Wang, Q. Yang, C. Zhong, W. Yang, *Angew. Chem., Int. Ed.* **2015**, *54*, 15483.
- [29] M. Zeeshan, V. Nozari, M. B. Yagci, T. Isik, U. Unal, V. Ortalan, S. Keskin, A. Uzun, *J. Am. Chem. Soc.* **2018**, *140*, 10113.
- [30] S. W. Kang, K. Char, J. H. Kim, C. K. Kim, Y. S. Kang, *Chem. Mater.* **2006**, *18*, 1789.

- [31] J. Shen, G. Liu, K. Huang, Z. Chu, W. Jin, N. Xu, *ACS Nano* **2016**, *10*, 3398.
- [32] a) W. L. Xu, C. Fang, F. Zhou, Z. Song, Q. Liu, R. Qiao, M. Yu, *Nano Lett.* **2017**, *17*, 2928; b) V. Saraswat, R. M. Jacobberger, J. S. Ostrander, C. L. Hummell, A. J. Way, J. Wang, M. T. Zanni, M. S. Arnold, *ACS Nano* **2018**, *12*, 7855.
- [33] a) J. Shen, G. Liu, K. Huang, W. Jin, K.-R. Lee, N. Xu, *Angew. Chem.* **2015**, *127*, 588; b) C. Chi, X. Wang, Y. Peng, Y. Qian, Z. Hu, J. Dong, D. Zhao, *Chem. Mater.* **2016**, *28*, 2921; c) H. W. Kim, H. W. Yoon, S.-M. Yoon, B. M. Yoo, B. K. Ahn, Y. H. Cho, H. J. Shin, H. Yang, U. Paik, S. Kwon, J.-Y. Choi, H. B. Park, *Science* **2013**, *342*, 91.